First-principles calculations for the magnetic phase diagram in electron-doped $CaMnO_3$ under compressive and tensile strains

Hiroshi Tsukahara,[1,2] Shoji Ishibashi,[1,2] and Kiyoyuki Terakura[1,3,2]

[1]*Research Institute for Computational Sciences (RICS), National Institute of Advanced Industrial Science and Technology (AIST), 1-1-1 Umezono, Tsukuba, Ibaraki 305-8568, Japan*

[2]*JST, CREST, 4-1-8 Honcho, Kawaguchi, Saitama 332-0012, Japan*

[3]*Research Center for Integrated Science (RCIS), Japan Advanced Institute of Science and Technology (JAIST), 1-1 Asahidai, Nomi, Ishikawa 923-1292, Japan*

(Received 24 November 2009; revised manuscript received 22 February 2010; published 11 June 2010)

We study how compressive and tensile strains affect a magnetic phase transition in electron-doped $CaMnO_3$ using density-functional theory calculation. In this system, distortion of oxygen octahedrons around Mn atoms and slight occupancy of e_g orbitals play important roles in the stability of various magnetic phases. Without strain, the magnetic phase transition occurs nearly at the same number of doped electrons as the experimental one. Under both compressive and tensile strains, a smaller amount of doped electrons causes the magnetic phase transition as compared to that without strain. Note that the compressive and tensile strains stabilize different phases after the phase transition. These features suggest that we can control the magnetic phase with electron doping and strain.

DOI: 10.1103/PhysRevB.81.214108 PACS number(s): 71.15.Mb, 75.10.Lp, 75.30.Kz, 75.47.Lx

I. INTRODUCTION

Perovskite manganites have been under intensive study because of their attractive electronic and magnetic properties such as colossal magnetoresistance, metal-insulator transition, and magnetic phase transition. A typical example is hole-doped manganites such as $La_{1-x}Ca_xMnO_3$ and $Pr_{1-x}Sr_xMnO_3$.[1–10] A large number of studies have been devoted to these system. On the other hand, there have been few studies on electron-doped manganites as compared to hole-doped ones.[10–15]

$Ca_{1-x}Ce_xMnO_3$ (Refs. 16 and 17) is one of electron-doped manganites with undoped $CaMnO_3$ being an antiferromagnetic (AFM) insulator. The substitution of Ce^{4+} for Ca^{2+} provides two electrons into e_g orbitals of Mn atom. In the bulk, a small amount of Ce doping causes consecutive phase transitions: from collinear G-type AFM insulator to canted G-type AFM metal at $x \sim 0.01$ and from canted G-type AFM to collinear C-type AFM insulator at $x \sim 0.07$ (see Sec. II for AFM magnetic structures). Interestingly, transport properties of the thin film are different from those of bulk materials due to epitaxial strains.[18] This feature suggests a possibility that we can control various properties such as magnetic phase transition with a small amount of electron doping and strain.

In previous first-principles calculations, structural, electronic, and magnetic properties of $CaMnO_3$ were investigated.[19–28] However no report is available so far on the effects of electron doping and strains on the electronic and magnetic properties. As there is a strong correlation among orbital, spin, and lattice in perovskite transition metal oxides, small change in orbital occupation by doping and also small change in lattice parameters by strain will strongly influence the electronic and magnetic properties of $CaMnO_3$.

In this paper, we will demonstrate that $CaMnO_3$ can have a very rich phase diagram in the space spanned by strain and electron doping and analyze the basic mechanisms controlling the phase diagram. Our study is based on the first-principles density-functional calculations as explained in the next section.

II. COMPUTATIONAL DETAILS

All the calculations were done with QMAS (Quantum MAterials Simulator), which is based on the projector augmented wave method[29,30] with the plane-wave basis set. As for exchange and correlation energies of electrons, we used the PBE version of generalized gradient approximation (GGA).[31] See Ref. 32 for the comment on the use of GGA rather than GGA+U in the present work. Convergence criteria for the stress and the atomic force were 1.0×10^{-6} Ry/bohr^3 and 1.0×10^{-4} Ry/bohr, respectively. The plane-wave energy cutoff for the wave-function expansion

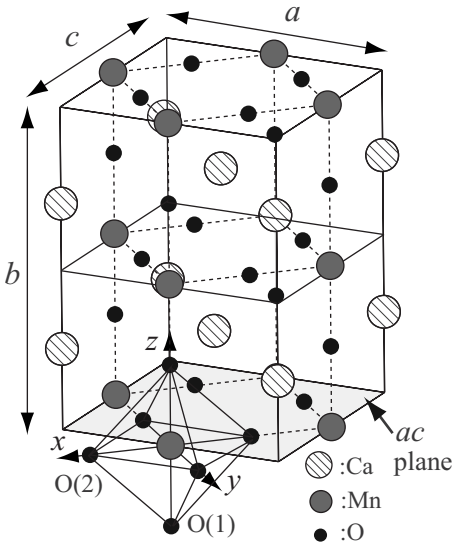

FIG. 1. A schematic illustration of the unit cell for orthorhombic $CaMnO_3$. Note the relation between (x,y,z) and (a,b,c).

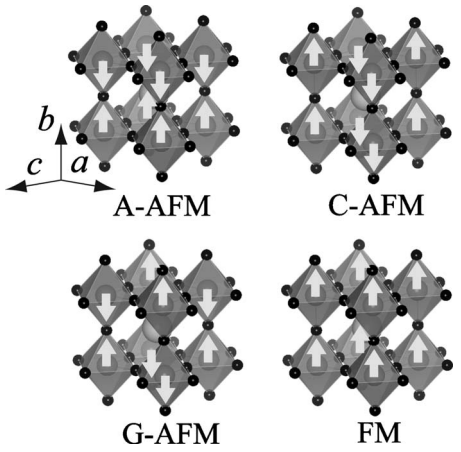

FIG. 2. A schematic illustration of magnetic structures.

was set to 40.0 Ry. The sampling **k** points were set to 8 $\times 6 \times 8$ in the whole Brillouin zone. In the calculations for the electron-doped system $Ca_{1-x}Ce_xMnO_3$, we adjusted only the number of valence electrons without taking account of the difference in the pseudopotential between Ca^{2+} and Ce^{4+}. The charge neutrality of the system is guaranteed by using a uniform background of positive charge. This is certainly a rather crude approximation neglecting the randomness in the potential and ionic size difference. The description of the insulating phase appearing frequently (but not observed in the present system) in the low-doping regime is beyond the scope of the present work. Nonetheless, as the basic physics of perovskite manganites is mainly controlled by the occupation of Mn $3d$ orbitals and the hybridization between Mn $3d$ and O $2p$ orbitals, the present approximation will capture the basic aspects of doping and pressure effects on the present system. More elaborate calculations taking account of different pseudopotentials for Ca^{2+} and Ce^{4+} are the next step task.

In order to check the performance of approximations and the validity of parameter sets in the present calculation, we did careful analysis of the crystal structure of bulk $CaMnO_3$ by fully optimizing the lattice constants and the atomic positions. For simulating the case where $CaMnO_3$ film is grown on a given substrate, the lattice constants in the ac plane were fixed to those of the substrate and only the one along the b axis was optimized. The definition of a, b, and c axes is given in Fig. 1. As for magnetic structures, we considered typical four cases, which are A-, C-, and G-type antiferromagnetic (A-AFM, C-AFM, and G-AFM) structures and ferromagnetic (FM) one shown in Fig. 2. Only the collinear magnetic ordering is treated in the present work. The Mn atoms were kept at the $4b$ position and the force acting on them was smaller than the convergence criterion in all cases studied in this work.

TABLE I. The theoretical and the experimental lattice constants and nonequivalent atomic positions in $CaMnO_3$. The magnetic ordering is G-AFM and the crystal structure is orthorhombic *Pnma*. u, v, and w are internal coordinates of the a, b, and c axes, respectively. Wyckoff positions are represented in parentheses. $d_{\text{Mn-O(1)}}$ and $d_{\text{Mn-O(2)}}$ are the bond length between Mn and O(1) and the one between Mn and O(2). ∠Mn-O(1)-Mn and ∠Mn-O(2)-Mn are the bond angles. m is the magnetic moment and E_{gap} is the band gap.

Lattice constants	This work	LDA[d]	Expt.[e]
a (Å)	5.3296	5.287	5.2791
b (Å)	7.4853	7.498	7.4566
c (Å)	5.2829	5.235	5.2706
Atomic positions			
Ca($4c$)			
u	0.0459	0.040	0.0323
v	0.2500	0.250	0.2500
w	−0.0078	−0.008	−0.0093
Mn($4b$)			
u	0.000	0.000	0.000
v	0.000	0.000	0.000
w	0.500	0.500	0.500
O(1)($4c$)			
u	0.4873	0.485	0.4932
v	0.2500	0.250	0.2500
w	0.0071	0.071	0.0683
O(2)($8d$)			
u	0.2889	0.287	0.2904
v	0.0372	0.036	0.0302
w	−0.2901	−0.288	−0.2890
Bond lengths			
Mn-O(1) (Å)	1.9106		1.899
Mn-O(2) (Å)	1.9213		1.907
	1.9179		1.896
Bond angles			
∠Mn-O(1)-Mn	156.79		158.04
∠Mn-O(2)-Mn	155.54		157.44
Magnetic moment and band gap			
m (μ_B/Mn)	2.59	2.65[a]	2.44[b]
E_{gap} (eV)	0.78	0.8	3.1[c]

[a]Reference 27.
[b]Reference 9.
[c]Reference 34.
[d]Reference 28.
[e]Reference 17.

III. RESULTS AND DISCUSSION

A. Full structural optimization (bulk case)

For all the four magnetic structures studied in this work, the electronic structure of bulk $CaMnO_3$ is insulating with the majority-spin Mn t_{2g} orbitals fully occupied and the other Mn d orbitals unoccupied. In such a situation, the AFM superexchange[32,33] between neighboring Mn t_{2g} orbitals makes G-AFM the most stable. The crystal structure after

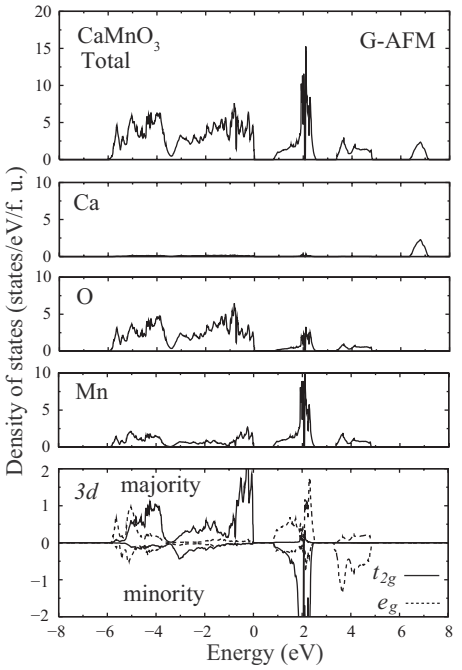

FIG. 3. The total density of states, the atom projected local densities of states and the partial densities of states for Mn 3*d* orbitals of $CaMnO_3$ with G-AFM per formula unit. The top of the valence band is taken as zero of energy.

optimization remains to be *Pnma*. Optimized lattice constants, atomic positions, bond lengths and angles, magnetic moment, and band gap are summarized in Table I. The structure parameters and the magnetic moment are in good agreement with those in the density-functional theory (DFT) calculation using local-density approximation (LDA) (Ref. 28)

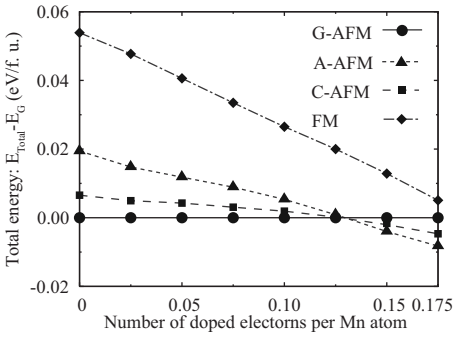

FIG. 4. The total energies of different magnetic structures per formula unit with reference to that of G-AFM.

and experiments.[9,17] As usual, the DFT calculations give a much smaller band gap than the experimental one, which was observed in the paramagnetic state at room temperature. Figure 3 shows the total density of states (DOS) and the local DOSs for Ca, O, and Mn atoms and the partial DOSs (pDOS) of Mn 3*d* orbitals for G-AFM. The pDOS of Fig. 3 suggests that the doped electrons occupy primarily the majority-spin e_g orbitals.

Next, we study the electronic, magnetic, and structural properties of electron-doped $CaMnO_3$ by optimizing full crystal structure. Figure 4 shows calculated total energies of the four magnetic states for the electron-doped $CaMnO_3$ with reference to the total energy of the G-AFM state as a function of number of doped electrons per Mn atom (N_e). For the undoped case (N_e=0.0), as the nearest-neighbor magnetic coupling is AFM, the magnetic structure with more FM pairs has higher energy. From the pDOS of Mn 3*d* orbitals at N_e =0.175 shown in Fig. 5, it is clear that the doped electrons fill mainly the e_g orbitals. As we dope electrons to e_g orbitals,

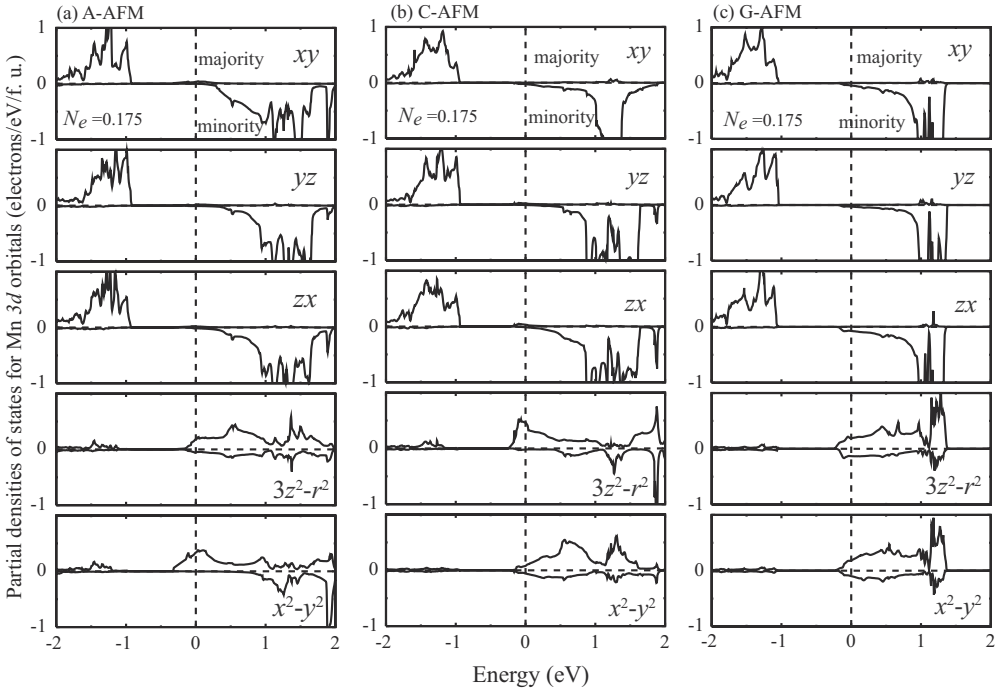

FIG. 5. The partial densities of states for Mn 3*d* orbitals per formula unit at N_e=0.175 in the case of (a) A-AFM, (b) C-AFM, and (c) G-AFM.

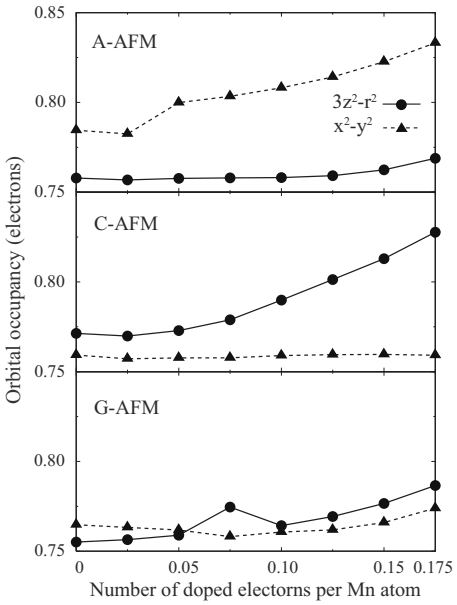

FIG. 6. The occupancy for e_g orbitals as a function of number of doped electrons per Mn atom for three different AFM structures.

FM double exchange[35] starts to operate and the magnetic structure with more FM pairs becomes relatively more stable. This tendency is clearly seen in Fig. 4 and all the three AFM structures are nearly degenerate at $N_e \simeq 0.125$. Further increase in N_e makes A-AFM the lowest in energy and C-AFM the second lowest. Some detailed aspects of the N_e dependence of electronic structure and crystal structure are discussed below. As we discuss the case for $N_e \leq 0.175$ where the FM structure has the highest total energy, most of the results shown below are only for three AFM structures.

Figure 6 shows for three different AFM structures how each e_g orbital is occupied as electrons are doped. The variations in bond lengths and bond angles are shown in Fig. 7 and those for the lattice constants are shown in Fig. 8. In order to understand these results, we first discuss the undoped case (N_e=0.0). As seen from Figs. 7(a) and 7(b), the atomic structure of the ground-state magnetic ordering G-AFM is characterized with the smaller bond angle in the *ac* plane [∠Mn-O(2)-Mn] than that along the *b* axis [∠Mn-O(1)-Mn] and also with the nearly same bond distance between in plane ($\langle d_{\text{Mn-O(2)}} \rangle$) and out of plane ($d_{\text{Mn-O(1)}}$). Note that there are two different Mn-O(2) bonds in the *ac* plane and that $\langle d_{\text{Mn-O(2)}} \rangle$ denotes the average of the two bond lengths. If the magnetic ordering is C-AFM, the bond length $d_{\text{Mn-O(1)}}$ becomes longer and the bond angle ∠Mn-O(1)-Mn becomes smaller compared with those in G-AFM because of absence of energy gain by AFM superexchange between Mn atoms along the *b* axis in C-AFM. Similarly in A-AFM where the magnetic ordering is FM in the *ac* plane, the bonds $d_{\text{Mn-O(2)}}$ are elongated and the bond angle ∠Mn-O(2)-Mn becomes smaller. The orbital population of e_g orbitals in Fig. 6 is correlated with the structural details of Fig. 7. For the undoped case (N_e=0.0), the orbital population is determined by the contributions of e_g orbitals mixed into the Mn majority-spin t_{2g} bands and the oxygen *p* bands. However the latter contribution is indeed tiny in the present system. The mixing between e_g orbitals and t_{2g} orbitals is possible through the deviation from 180° of the Mn-O-Mn bond angle. The larger orbital population for the x^2-y^2 orbital than that for the $3z^2-r^2$ orbital in A-AFM structure is due to the smaller bond angle ∠Mn-O(2)-Mn than ∠Mn-O(1)-Mn. Note that the *x*, *y*, and *z* directions are defined in Fig. 1. The orbital populations in G-AFM and C-AFM in Fig. 6 can be explained in a similar way.

The doping dependence of the orbital population and the structural details can be explained straightforwardly. Although we discuss only the A-AFM case as an example, similar arguments hold for other magnetic structures. In the A-AFM structure, the x^2-y^2 band will be wider than the $3z^2-r^2$ band because of the FM spin ordering in the *ac* plane. In addition to this, the larger $\langle d_{\text{Mn-O(2)}} \rangle$ than $d_{\text{Mn-O(1)}}$ makes the position of the (antibonding) x^2-y^2 band lower in energy. Due to these facts, the bottom of the conduction band is dominated by the x^2-y^2 orbital. These features are clearly

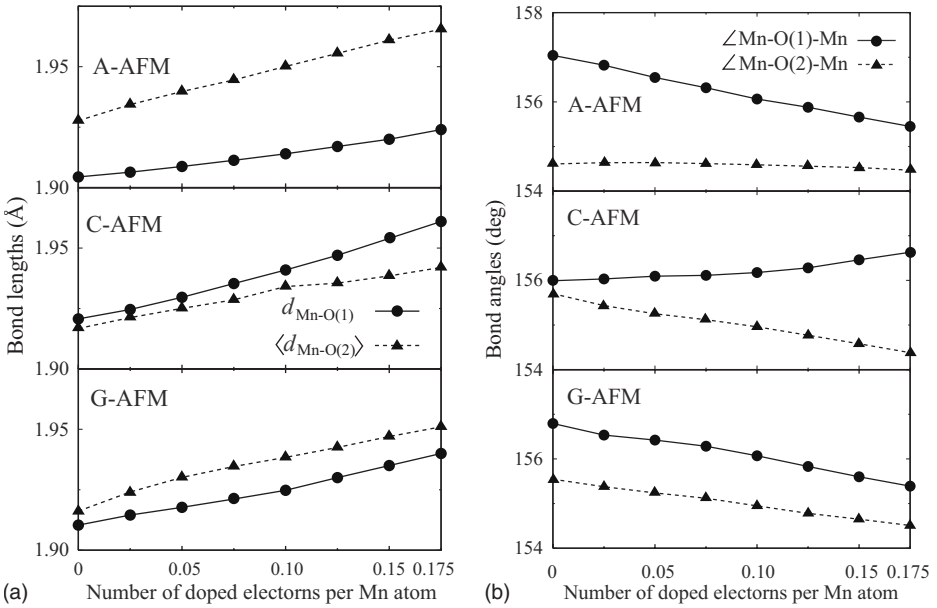

FIG. 7. (a) The bond lengths and (b) the bond angles as a function of number of doped electrons per Mn atom for three different AFM structures.

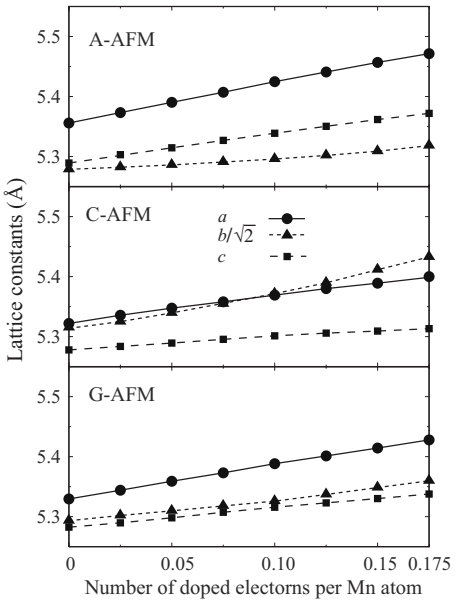

FIG. 8. The lattice constants as a function of number of doped electrons per Mn atom for three different AFM structures.

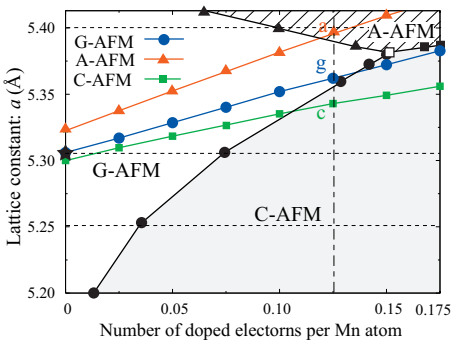

FIG. 9. (Color) The phase diagram of the electron-doped $CaMnO_3$ under strain. a is the in-plane lattice constant and filled black circles, triangles, and squares indicate calculated boundary points between G-AFM and C-AFM, between G-AFM and C-AFM, and between A-AFM and C-AFM, respectively. At the open square, the total energies for G-, A-, and C-AFM are almost the same. The filled black star denotes the lattice constant which equals to that undoped $CaMnO_3$. The lines connecting blue circles, red triangles, and green squares are the mean in-plane lattice constant for the bulk case of G-, A-, and C-AFM, respectively, as a function of number of doped electrons per Mn atom.

seen in Fig. 5. Therefore doped electrons occupy more the x^2-y^2 orbital than the $3z^2-r^2$ orbital. Then, more population of the d orbital which has the p-d antibonding character leads to stronger elongation of the particular bond $\langle d_{\text{Mn-O(2)}}\rangle$. The insensitivity of ∠Mn-O(2)-Mn to N_e may be due to the balance between the elongation of $\langle d_{\text{Mn-O(2)}}\rangle$ which may have a tendency toward decrease in ∠Mn-O(2)-Mn and the stronger stability of FM ordering in the ac plane which may have a tendency toward increase in ∠Mn-O(2)-Mn.

Before closing this section, we would like to make some comments on the comparison between our result and experimental observation. One clear discrepancy between them is that the actual observed transition is from canted G-AFM in *Pnma* crystal symmetry to C-AFM in $P2_1/m$ crystal symmetry[16] at $0.15<N_e\leq 0.2$ while our calculation predicts the transition from G-AFM to A-AFM both in *Pnma* crystal structure at $N_e=0.125$. As our calculation is restricted to only collinear spin arrangement, the treatment of canted G-AFM is beyond the scope of the present work. It may be reasonable that the transition occurs at smaller N_e in the calculation than that in the experiment because of the neglect of canted G-AFM. However, the relative stability between A-AFM and C-AFM in the doped system should be examined more carefully. In the present calculation, we ignored the difference in pseudopotential between Ca^{2+} and Ce^{4+} and therefore ignored the ionic size difference also (1.48 Å for Ca^{2+} and 1.28 Å for Ce^{4+}). If the ionic size of A-site cation becomes smaller, the rotation and tilt of MnO_6 octahedron will be more pronounced and the relative stability of $P2_1/m$ will be enhanced. In order to see the effect of subtle difference in the crystal structure on the stability of magnetic ordering, we made the following analysis. In the total-energy calculations at $N_e=0.175$ for the four magnetic structures, the internal coordinates (u, v, and w) for every atom are constrained to be the experimental ones at $N_e=0.2$ keeping the lattice frameworks the same as those of the full optimization for *Pnma* at $N_e=0.175$. Total energies with reference to the total energy of G-AFM are summarized in Table II. Although the result is rather subtle, this calculation suggests that C-AFM is indeed stabilized more strongly than A-AFM in the above fictitious crystal structure of $P2_1/m$.

TABLE II. The total energies per formula unit with reference to that of G-AFM using theoretical lattice constants. Internal coordinates are theoretical ones at $N_e=0.175$ for *Pnma* and experimental ones at $N_e=0.2$ for $P2_1/m$.

Pnma	A-AFM	C-AFM	G-AFM	FM
Total energy (eV)	−0.00828	−0.00468	0.0000	0.00508
$P2_1/m$				
Total energy (eV)	−0.00710	−0.00808	0.0000	0.01003

The variation in the structural parameters shown in Figs. 7 and 8 can also be compared with the observed ones.[16,17] As we neglected the ionic size difference between Ca^{2+} and Ce^{4+}, the detailed quantitative comparison may not be so meaningful. Anyway, it is important to note that, although Ce^{4+} has smaller ionic size than that of Ca^{2+}, not only the Mn-O bond lengths but also the lattice constants increase with N_e in both our calculation and the experiments.[16,17] However, reflecting the smaller ionic size of Ce^{4+}, the observed rate of increase in these lengths is about 1/2 or 1/3 of the calculated one.

B. Structural optimization with constraint (film grown on a substrate)

As mentioned in Sec. I, it was experimentally observed that a film grown epitaxially on a substrate exhibits different transport properties depending on the substrate lattice

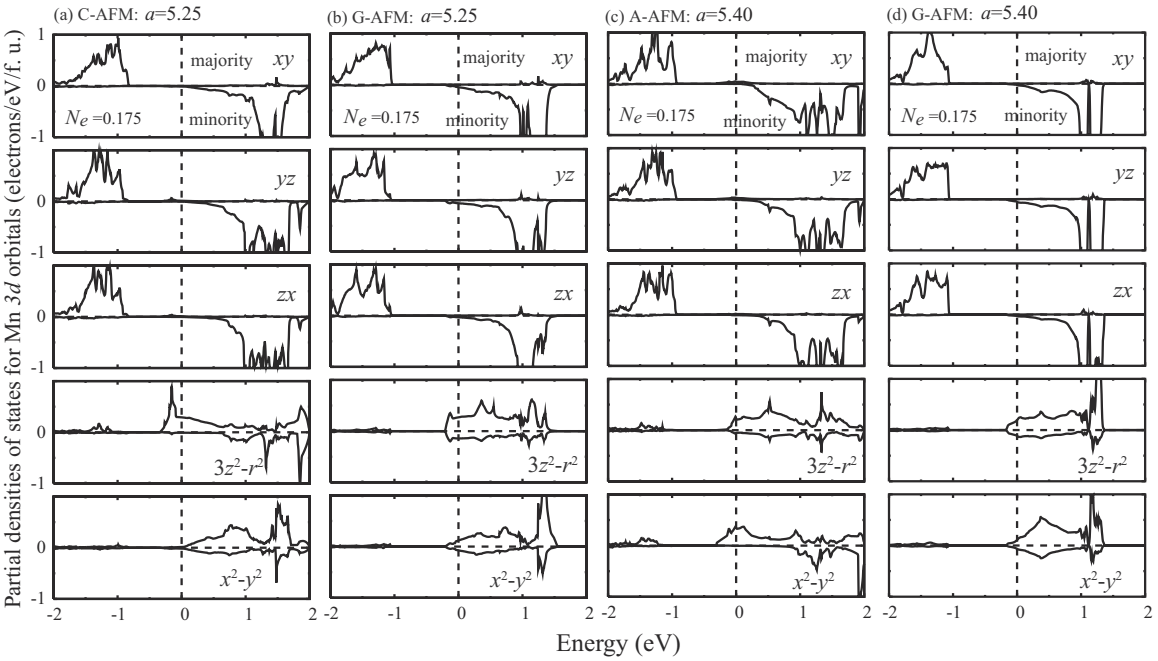

FIG. 10. The partial densities of states for Mn 3*d* orbitals at N_e=0.175. (a) and (b) are those of C- and G-AFM, respectively, at a =5.25 Å and (c) and (d) are those of A- and G-AFM, respectively, at a=5.40 Å.

constant.[18] As the in-plane lattice constants of the film are constrained to those of the substrate, we study in this section the effect of strain on the electronic and magnetic properties of $Ca_{1-x}Ce_xMnO_3$. As the substrates used experimentally are mostly cubic or pseudocubic, we assumed that the two lattice constants in the *ac* plane are the same.

The magnetic phase diagram in the space spanned by the in-plane lattice constant and N_e is shown in Fig. 9. In this figure, the average of the lattice constants a and c in the bulk $Ca_{1-x}Ce_xMnO_3$ with $N_e=2x$ for each of the three AFM structures is also plotted with blue circles (G-AFM), red triangles (A-AFM), and green squares (C-AFM). Similar analysis on phase diagram was given for $La_{1-x}Sr_xMnO_3$ (Refs. 36–39) and the general feature that the shorter (longer) in-plane lattice constant has a tendency toward stabilization of C-AFM (A-AFM) is common to both cases. In the recent work on Ba doped $LaMnO_3$,[40] the Ba doping effect on the relative stability among different magnetic orderings was studied for a tetragonal lattice with a basal plane lattice constant fixed to that of $SrTiO_3$. However, tilting and rotation of MnO_6 octahedron were not taken into account. In the present case, the AFM superexchange strongly stabilizes G-AFM at N_e=0.0 and therefore the region of stable G-AFM is wide. As N_e increases, FM double exchange becomes stronger and the G-AFM region becomes narrower due to the expansion of the A-AFM and C-AFM regions.

It may be meaningful to make a comment on the relation between Figs. 4 and 9. In Fig. 4, the three AFM structures have nearly the same total energy at N_e=0.125. This situation corresponds to the points denoted with a, g, and c in Fig. 9. As different AFM structures at their corresponding points have different lattice constants, a is in the A-AFM region, g in the G-AFM region, and c in the C-AFM region. On the other hand, the point denoted with an open square in Fig. 9 is a triple point in the phase diagram at which three AFM structures have the same energy and the same in-plane lattice constant. Therefore, if the system may be close to this triple point, strong magnetic quantum fluctuation may be expected.

It is also important to note that the path in the phase space of electron doping is different between the bulk case and the epitaxial grown films. For bulk case, the path of electron doping is along the line connecting the blue circles until coming up to the point g and the path jumps to the line connecting red triangles as suggested by Fig. 4. On the other hand, even if we grow a film on the substrate whose lattice

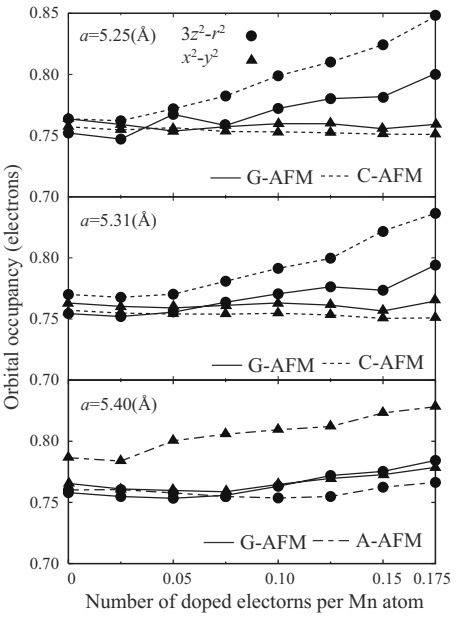

FIG. 11. The occupancy of e_g orbitals under the strains as a function of number of doped electrons per Mn atom.

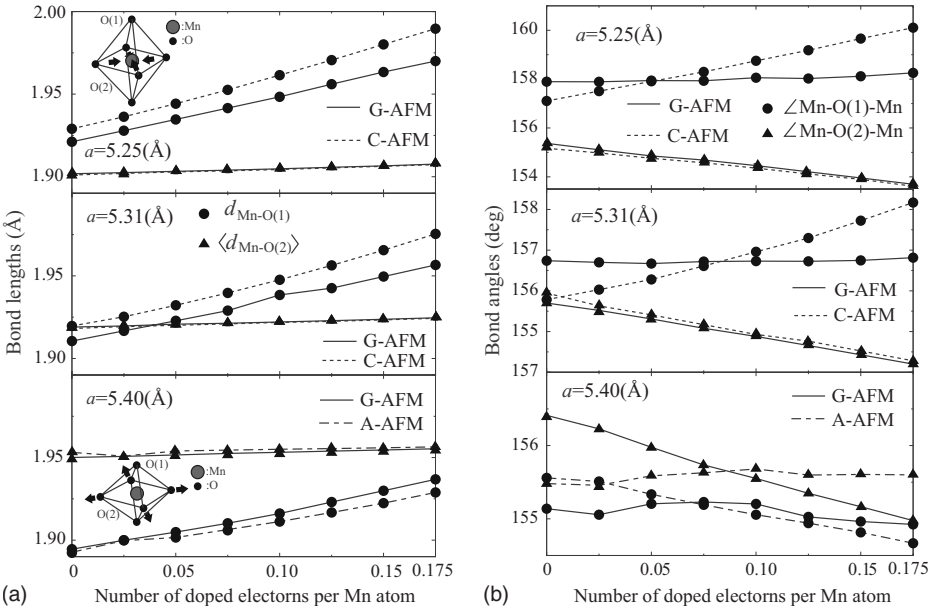

FIG. 12. The bond lengths and angles under the strains as a function of number of doped electrons per Mn atom. An inset illustrates the distortion of the oxygen octahedron around Mn atom.

constant is equal to that of undoped $CaMnO_3$, the path of electron doping is along the thin dotted horizontal line with the in-plane lattice constant of 5.31 Å. Then, this path hits the boundary of C-AFM region already at $N_e=0.075$ rather than $N_e=0.125$. Therefore, the phase transition to C-AFM occurs at much smaller doping level. On the other hand, in order to realize the stable A-AFM by doping, we have to use a substrate with much larger in-plane lattice constant.

Figure 10 shows pDOS of Mn $3d$ orbitals at $N_e=0.175$ for different magnetic structures under compressive strain [(a) and (b)] and tensile strain [(c) and (d)] in the ac plane. Similarly to the case of bulk system as shown in Fig. 5, doped electrons mostly enter e_g orbitals. However, the orbital occupancy (Fig. 11), bond lengths [Fig. 12(a)], and bond angles [Fig. 12(b)] as a function of N_e for epitaxially grown film behave quite differently from those of bulk case shown in Figs. 6 and 7. We discuss their behavior in relation to the phase diagram of Fig. 9. In Fig. 11 we show the occupancy of each e_g orbital in different AFM structures for three in-plane lattice constants corresponding to three thin horizontal lines in Fig. 9. Clearly, $a=5.25$ Å corresponds to entirely a compressive strain case, $a=5.31$ Å the same lattice constant of undoped $CaMnO_3$ and $a=5.40$ Å a tensile strain case. Figure 10 shows pDOS of Mn $3d$ orbitals under the compressive and tensile strain.

For the case of compressive strain, x^2-y^2 orbital will be shifted upward in energy due to stronger p-d hybridization within ac plane and doped electrons will mostly occupy $3z^2-r^2$ orbital. Moreover, the bandwidth of $3z^2-r^2$ orbital will be wider in C-AFM than G-AFM and doped electrons will more preferentially occupy this orbital. These features are clearly from pDOS of Mn $3d$ orbitals shown in Fig. 10 and stabilize C-AFM more strongly. The behaviors of Mn-O bond lengths and bond angles are mutually correlated with the behavior of orbital population and can be easily understood. It is obvious that, in the case of compressive strain, the in-plane bond length $\langle d_{\text{Mn-O(2)}}\rangle$ is smaller and shows little variation with N_e, while the out-of-plane bond length $d_{\text{Mn-O(1)}}$ is larger and increases with N_e because of the population increase in $3z^2-r^2$ orbital which corresponds to the p-d antibonding state. The strong increase in the bond angle $\angle$Mn-O(1)-Mn with N_e in C-AFM [see Fig. 12(b)] helps to enhance the FM double exchange. Even if the substrate is undoped $CaMnO_3$, the lattice of the epitaxial film of $Ca_{1-x}Ce_xMnO_3$ tends to expand with x and the film undergoes in-plane compressive strain.

The situation in the case of tensile strain is shown for $a=5.40$ Å in Figs. 11 and 12. In this case, x^2-y^2 orbital will be shifted downward in energy and will be predominantly populated by doped electrons particularly in A-AFM because of its wider bandwidth than that of G-AFM. Higher population of x^2-y^2 orbital may make $\langle d_{\text{Mn-O(2)}}\rangle$ longer in the absence of any constraint but $\langle d_{\text{Mn-O(2)}}\rangle$ is nearly unchanged due to the fixed in-plane lattice constant. The difference in the behavior of structural parameters between A-AFM and G-AFM can be seen in the bond angle shown in Fig. 12(b). Although $\angle$Mn-O(2)-Mn decreases significantly with N_e in G-AFM, it remains nearly constant in A-AFM and helps FM double exchange operate in the in plane.

IV. CONCLUSION

We performed first-principles electronic calculations in GGA to study the magnetic phase diagram of electron-doped $CaMnO_3$ with nonconstrained bulk condition and with constraint on the ac plane lattice constant. The latter case corresponds to films epitaxially grown on cubic or pseudocubic substrate. For the bulk case, our calculation reproduces the ground-state magnetic structure G-AFM and predicts the stability of A-AFM structure beyond $N_e=0.125$ with N_e being the number of doped electrons per Mn atom. In the experiment on $Ca_{1-x}Ce_xMnO_3$, the C-AFM structure becomes stable with increase in Ce content. We analyzed the possible reason for the discrepancy between our calculation and the experiment. In the present calculation, the effect of Ce doping was simply regarded as electron addition and the ionic size difference between Ca^{2+} and Ce^{4+} was not taken into account. Our analysis clearly suggests that the neglect of the

ionic size difference may be the main source of the above discrepancy.

In order to simulate the case of $Ca_{1-x}Ce_xMnO_3$ films epitaxially grown on some cubic or psuedocubic substrates, the in-plane lattice constants were constrained to a given lattice constant of the substrate and other structural parameters were optimized. By doing this, we obtained magnetic phase diagram in the space spanned by N_e and the in-plane lattice constant. This phase diagram suggests that in the case of in-plane compressive strain the region of stable C-AFM becomes wide. Even if we use a substrate whose lattice constant is the same as undoped $CaMnO_3$, electron doping will expand the lattice and therefore the epitaxially grown film may undergo in-plane compressive strain. In contrast to the case of bulk material where stability of A-AFM starts at $N_e=0.125$, the stability of C-AFM (rather than A-AFM) starts already at $N_e=0.075$. On the other hand, A-AFM becomes hard to be realized.

ACKNOWLEDGMENTS

The authors thank P.-H. Xiang, H. Sato, I. H. Inoue, A. Sawa, H. Akoh, N. Zhong, H. Shima, H. Akinaga, Z.-M. Hou, T. Tamura, H.-F. Weng, T. Hashimoto, and N. Orita for fruitful discussions and Y. Shiihara, S. Tanaka, and M. Kohyama for their help in developing our computational code QMAS. The calculations were performed using the AIST Super Cluster and the T2K Open Supercomputer Alliance at the Center for Computational Science of the University of Tsukuba.

[1] S. Jin, T. H. Tiefel, M. McCormack, R. A. Fastnacht, R. Ramesh, and L. H. Chen, Science **264**, 413 (1994).
[2] Y. Moritomo, A. Asamitsu, and Y. Tokura, Phys. Rev. B **51**, 16491 (1995).
[3] A. Urushibara, Y. Moritomo, T. Arima, A. Asamitsu, G. Kido, and Y. Tokura, Phys. Rev. B **51**, 14103 (1995).
[4] Y. Tomioka, A. Asamitsu, Y. Moritomo, and Y. Tokura, J. Phys. Soc. Jpn. **64**, 3626 (1995).
[5] Y. Tokura, H. Kuwahara, Y. Moritomo, Y. Tomioka, and A. Asamitsu, Phys. Rev. Lett. **76**, 3184 (1996).
[6] J. Z. Sun, W. J. Gallagher, P. R. Duncombe, L. Krusin-Elbaum, R. A. Altman, A. Gupta, Y. Lu, G. Q. Gong, and G. Xiao, Appl. Phys. Lett. **69**, 3266 (1996).
[7] H. Yamada *et al.*, Science **305**, 646 (2004).
[8] B. Raveau, A. Maignan, C. Martin, and M. Hervieu, Chem. Mater. **10**, 2641 (1998).
[9] E. O. Wollan and W. C. Koehler, Phys. Rev. **100**, 545 (1955).
[10] C. N. R. Rao, J. Phys. Chem. B **104**, 5877 (2000).
[11] A. L. Cornelius, B. E. Light, and J. J. Neumeier, Phys. Rev. B **68**, 014403 (2003).
[12] C. R. Wiebe, J. E. Greedan, J. S. Gardner, Z. Zeng, and M. Greenblatt, Phys. Rev. B **64**, 064421 (2001).
[13] J. J. Neumeier and J. L. Cohn, Phys. Rev. B **61**, 14319 (2000).
[14] C. D. Ling, E. Granado, J. J. Neumeier, J. W. Lynn, and D. N. Argyriou, Phys. Rev. B **68**, 134439 (2003).
[15] E. Granado, C. D. Ling, J. J. Neumeier, J. W. Lynn, and D. N. Argyriou, Phys. Rev. B **68**, 134440 (2003).
[16] E. N. Caspi, M. Avdeev, S. Short, J. D. Jorgensen, M. V. Lobanov, Z. Zeng, M. Greenblatt, P. Thiyagarajan, C. E. Botez, and P. W. Stephens, Phys. Rev. B **69**, 104402 (2004).
[17] M. E. Melo Jorge, M. R. Nunes, R. Silva Maria, and D. Sousa, Chem. Mater. **17**, 2069 (2005).
[18] P.-H. Xiang, H. Yamada, A. Sawa, and H. Akoh, Appl. Phys. Lett. **94**, 062109 (2009).
[19] W. E. Pickett and D. J. Singh, Phys. Rev. B **53**, 1146 (1996).
[20] S. Satpathy, Z. S. Popović, and F. R. Vukajlović, Phys. Rev. Lett. **76**, 960 (1996).
[21] N. A. Hill and K. M. Rabe, Phys. Rev. B **59**, 8759 (1999).
[22] A. Filippetti and W. E. Pickett, Phys. Rev. Lett. **83**, 4184 (1999).
[23] A. Filippetti and W. E. Pickett, Phys. Rev. B **62**, 11571 (2000).
[24] T. Saha-Dasgupta and S. Satpathy, J. Phys.: Condens. Matter **15**, 1685 (2003).
[25] A. Filippetti and N. A. Spaldin, Phys. Rev. B **68**, 045111 (2003).
[26] W. Luo, A. Franceschetti, M. Varela, J. Tao, S. J. Pennycook, and S. T. Pantelides, Phys. Rev. Lett. **99**, 036402 (2007).
[27] C. Cardoso *et al.*, J. Phys.: Condens. Matter **20**, 035202 (2008).
[28] S. Bhattacharjee, E. Bousquet, and P. Ghosez, J. Phys.: Condens. Matter **20**, 255229 (2008).
[29] P. E. Blöchl, Phys. Rev. B **50**, 17953 (1994).
[30] G. Kresse and D. Joubert, Phys. Rev. B **59**, 1758 (1999).
[31] J. P. Perdew, K. Burke, and M. Ernzerhof, Phys. Rev. Lett. **77**, 3865 (1996).
[32] J. Kanamori, J. Phys. Chem. Solids **10**, 87 (1959). We make a brief comment on the use of GGA rather than GGA+U in the present work. As seen from the significant underestimation of band gap (Table I), the use of GGA may be more appropriate in the present system. However, the effect of U is much stronger on t_{2g} states than e_g states due to the different strength of p-d hybridization. Therefore, the band gap increase caused by U may be mostly contributed by the lowing of the valence-band top with strong t_{2g} character. As pointed out in the following section, the doped electrons mostly enter e_g states in the current system and the effect of U will not modify significantly the results obtained by GGA. This expectation is supported by the previous work (Ref. 36) in which the experimental phase diagram of $La_{1-x}Sr_xMnO_3$ is correctly reproduced by GGA.
[33] P. W. Anderson, Phys. Rev. **79**, 350 (1950).
[34] J. H. Jung, K. H. Kim, D. J. Eom, T. W. Noh, E. J. Choi, J. Yu, Y. S. Kwon, and Y. Chung, Phys. Rev. B **55**, 15489 (1997).
[35] P. W. Anderson and H. Hasegawa, Phys. Rev. **100**, 675 (1955).
[36] Z. Fang, I. V. Solovyev, and K. Terakura, Phys. Rev. Lett. **84**, 3169 (2000).
[37] Z. Fang and K. Terakura, J. Phys. Soc. Jpn. **70**, 3356 (2001).
[38] G. Colizzi, A. Filippetti, F. Cossu, and V. Fiorentini, Phys. Rev. B **78**, 235122 (2008).
[39] G. Colizzi, A. Filippetti, F. Cossu, and V. Fiorentini, Eur. Phys. J. B **70**, 343 (2009).
[40] J. D. Burton and E. Y. Tsymbal, Phys. Rev. B **80**, 174406 (2009).